

Research article

Simulation studies on the densification behaviour of sintered aluminium preforms

Md. Ahasan^{a*}, M.J. Davidson^b, Asit Kumar Khanra^c

^{a,b}Mechanical Engineering Department, National Institute of Technology, Warangal, India

^cMetallurgical & Materials Engineering Department, National Institute of Technology, Warangal, India

Received 24 June 2013

Revised 20 November 2013

Accepted 24 November 2013

Abstract

The densification behavior of sintered aluminium has been investigated by performing simulation studies using DEFORM 2D software. The results have been compared with the experimental values. The deformation characteristics of the sintered preforms have been studied and the relationship between the various stresses such as true stress, true strain, hoop stress, hoop strain, hydrostatic stress, hydrostatic strain, effective stress, effective strain and relative density in both the experimental and simulations has been discussed for uniaxial, plane stress and triaxial stress state conditions. A good agreement is found between the experimental and simulation results.

©2013 Usak University all rights reserved.

Keywords: Simulation, densification, sintered preforms, compression test, deform-2D

1. Introduction

Powder forging is the process of making products of different shapes from compacts of pressed and sintered powder samples. The pressing will be done by compacting process, and the sintering will be done by heating the pressed samples in controlled environment. It is a near net shape manufacturing process and, as such, the process has the capability to greatly save machining cost, and can improve material utilization [1-2]. The studies on the deformation behaviour of sintered porous materials were started in the early 1960s. Hansen *et al.* [3] developed dispersion strengthened aluminium alloys by powder blending principles. Kuhn [4] performed a series of upsetting, bending, rolling and plane strain tests to assess the fracture behaviour of porous materials. Narayanasamy [5] performed cold upsetting tests on aluminium preforms. Park *et al.* [6] developed a constitutive relation involving Poisson's ratio, relative density and flow stress to predict the plastic deformation behaviour of porous metals. Selvakumar *et al.* [7] performed cold upsetting tests on sintered aluminium preforms to evaluate the work hardening characteristics. The instantaneous strain hardening exponent, n_i and the strength coefficient, k_i were calculated from the experiments and they observed that both n_i and k_i

*Corresponding author: Tel: +91 – 986 – 6305143

E-mail: mdahasankhan@gmail.com

DOI: 10.12748/ujms.201324254

reached a peak value when the packing density was at a low value. In recent years, a number of researchers have worked on the densification of powder preforms by upset forging technique.

Narayanasamy *et al.* [8] have studied the strain hardening behaviour of aluminium- iron powder composite preforms. The authors performed experiments on sintered powders of three different aspect ratios, different compositions of Fe and three different particle sizes. The experiments were done under various stress state conditions namely uniaxial, plane stress and triaxial stress states. The authors measured the strain hardening exponent, n_i and strength coefficient, k_i for different aspect ratios and for different compositions, and they concluded that the strength coefficient value (k_i) for small particles is high in the case of uniaxial stress condition compared with other stress state conditions. The hoop stress in the triaxial stress state was always found to be higher than the other two stress state conditions.

Zhang *et al.* [9] have developed a finite element method to analyze the deformation behaviour of sintered metals in forging. They have analyzed the effect of friction, height to diameter ratio, the initial relative density, and the shape of the preform on the forming limit. Cheng-Chao *et al.* [10] investigated the deformation behaviour of sintered porous materials of different aspect ratios and frictional conditions. Finite element analysis based simulations were performed to analyze the deformation behaviour. The authors formulated new forming limiting criteria, and showed that the fracture strain is directly proportional to the aspect ratio.

Even though large numbers of researchers have worked on the experimental investigation of porous materials, only a few researchers have attempted modelling studies on porous preforms. The present work is focused on the modelling of densification of sintered aluminium preforms when subjected to upsetting.

2.1. Experimental Work

The material used in this experimental work is finely pulverized, aluminium powder of particle size 47 micron obtained from SRL Labs Pvt. Ltd. Mumbai. The SEM photograph of the aluminium metal powder is shown in Fig. 1, the aluminium powder was used to prepare pure aluminium compacts of aspect ratio 1. Desired quantity of powder was weighed and poured into the die of size 15 mm diameter and 30 mm height, and the walls of the die was coated with zinc stearate. The preforms were made with a manual hydraulic press of 25 ton capacity under 3 MPa pressure. The compacts were sintered at a temperature of 500°C for 1 hour in a tubular furnace under controlled atmosphere (with argon gas). The sintered preforms were pressed again in a hydraulic press of 50 ton capacity incrementally to different height reductions. Gradual increase of load is applied to each billet upto crack initiation on the free surface. The top contact diameter (D_{top}), the bottom contact diameter (D_{bottom}), the bulge diameter (D_b) and the final height (H_f) were noted by using digital vernier calipers, and the density was measured by using Archimedes' principle for each of the deformed compacts before and after each step of deformation. From the measured dimensions, the normal stress (σ_z), normal strain (ϵ_z), hoop stress (σ_θ), hoop strain (ϵ_θ), hydrostatic stress (σ_m), effective stress (σ_{eff}) and effective strain (ϵ_{eff}) were calculated.

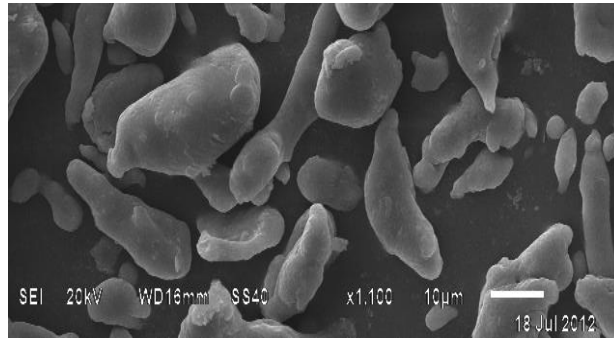


Fig.1 The SEM photograph of pure aluminium powder

2.2. FEA Simulations on the densification process

The experimental investigation was performed only for compacts of aspect ratio 1.0 (height to diameter ratio) and the analysis on compacts of aspect ratio 0.75 and 0.5 were performed on DEFORM-2D, an FEA based software. Fig. 2 shows the model that is created in DEFORM 2D. The load vs. displacement curve obtained from the simulation is given in Fig. 3. Chandrasekhar *et al.* [11] have applied this software to analyze the compaction pressure and deformation characteristics of sintered billets. In the present study, disc compression tests were performed to find the strain hardening index, n and the strength coefficient, k . The disc samples were prepared with an initial preform density of 0.88, and the preform was sintered at a temperature of 500°C for 1 hr. The disc samples used in this work are shown in Fig. 4. The flow curve was drawn from the disc compression tests and a new material corresponding to the experimentally determined flow stress was developed in the software. The geometry of the preform was created with an aspect ratio of 1, and modelled as porous material in the software. The modelled preform was assigned an initial preform density of 0.88. It was compressed between two platens made of rigid material. The friction between the workpiece and the dies was assumed as 0.3, and the speed of the ram was taken as 0.5 mm/sec. The deformation load, the displacement value, the top and bottom bulged diameters, and the density were noted down from the software.

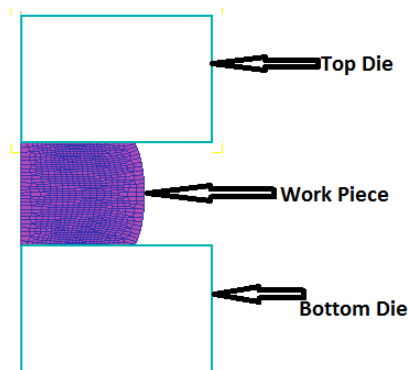


Fig. 2 The axisymmetric work piece between top die and bottom die after compression in DEFORM 2D

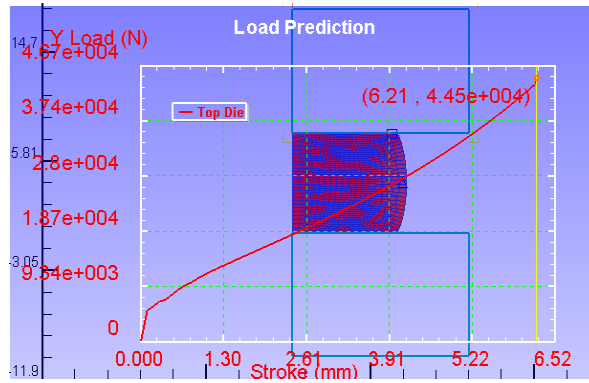


Fig. 3 The load versus displacement graph in DEFORM 2D



Fig. 4 Deformed billets

3. Theoretical Analysis

The expressions for the normal stress (σ_z), normal strain (ϵ_z), hoop stress (σ_θ), hoop strain (ϵ_θ), hydrostatic stress (σ_m), effective stress (σ_{eff}), and effective strain (ϵ_{eff}) were taken from Selvakumar *et al.* [7] and Narayanasamy *et al.* [8].

3.1. Uniaxial Stress State Condition

In the upsetting of P/M parts, the height decreases, the average density increases, and the various stress increases [12].

$$\text{Axial stress, } (\sigma_z) = \frac{\text{Load}}{\text{Contact Area}(Ac)} = -\sigma_{eff} \quad (1)$$

$$\text{Hoop stress, } \sigma_\theta = \sigma_r = 0 \quad (2)$$

$$\text{Hydrostatic stress, } \sigma_m = \sigma_z/3 \quad (3)$$

$$\text{Axial strain, } \epsilon_z = \ln\left(\frac{h_0}{h_f}\right) \quad (4)$$

$$\text{Effective strain, } \epsilon_{eff} = \ln\left(\frac{D_0}{D_f}\right) \quad (5)$$

$$\text{Formability stress index, } \beta = 3\sigma_m/\sigma_{eff} \quad (6)$$

3.2. Plane Stress State Condition

$$\text{Effective stress, } \sigma_{eff} = (0.5 + \alpha)[3(1 + \alpha + \alpha^2)]^{0.5} \sigma_z \quad (7)$$

$$\text{Poisson's ratio, } \alpha = \frac{\epsilon_\theta}{2\epsilon_z} \quad (8)$$

Since the radial stress, σ_r is zero at the free surface it follows from the rule that

$$\sigma_\theta = [(1 + 2\alpha)/(2 + \alpha)]\sigma_z \quad (9)$$

$$\text{Hoop strain, } \epsilon_\theta = \left[\frac{2D_b^2 + D_c^2}{3D_\theta^2} \right] \quad (10)$$

$$\text{New Poisson's ratio, } \vartheta = \left[\frac{\epsilon_\theta}{2\epsilon_z} \right] \quad (11)$$

$$\text{Hydrostatic stress, } \sigma_m = \left[\frac{\sigma_\theta + \sigma_z}{3} \right] \quad (12)$$

3.3. Triaxial Stress State Condition

$$\alpha = \frac{A}{B} \quad (13)$$

$$A = (2 + R^2)\sigma_\theta - R^2(\sigma_z + 2\sigma_\theta) \quad (14)$$

$$B = (2 + R^2)\sigma_z - R^2(\sigma_z + 2\sigma_\theta) \quad (15)$$

$$\text{Hoop stress, } \sigma_\theta = \left(\frac{(2\alpha + R^2)}{[2 - R^2 + 2R^2\alpha]} \right) \sigma_z \quad (16)$$

$$\text{Hydrostatic stress, } \sigma_m = \left[\frac{\sigma_z + 2\sigma_\theta}{3} \right] \quad (17)$$

$$\text{Effective stress, } \sigma_{eff} = \left[\frac{\sigma_z^2 + 2\sigma_\theta^2 - R^2(\sigma_\theta^2 + 2\sigma_z\sigma_\theta)}{2R^2 - 1} \right]^{1/2} \quad (18)$$

$$\text{Relative density, } R = \frac{\rho_f}{\rho_{th}} \quad (19)$$

$$\text{Instantaneous strain hardening, } n_i = \ln\left(\frac{\sigma_m}{\sigma_{m-1}}\right) / \ln\left(\frac{\epsilon_m}{\epsilon_{m-1}}\right) \quad (20)$$

$$\text{Instantaneous Strength, } k_i = \ln\left(\frac{\sigma_m}{\sigma_{m-1}}\right) / \ln\left(\frac{\epsilon_m^{n_i}}{\epsilon_{m-1}^{n_i}}\right) \quad (21)$$

4. Results and Discussions

Fig. 5 shows the relationship between the axial stress and the axial strain drawn from the experiments and the simulation. The axial stress increases as the axial strain is increased, and it is observed that both the simulation and experimental results are more or less similar, and at higher strains the result matches. The stress value increased as the aspect ratio of the preforms is decreased from 1 to 0.5. This is because, as the aspect ratio is decreased, less volume of the preforms will be receiving the deforming load and

therefore the stress increases. Additionally, the pores that are available on the preforms with lower aspect ratio will be less than that of the higher aspect ratio preforms, and hence, such pores will be closed faster than the higher aspect ratio preforms. Once more number of pores are closed, the stress will start increasing faster than that of its higher aspect ratio samples.

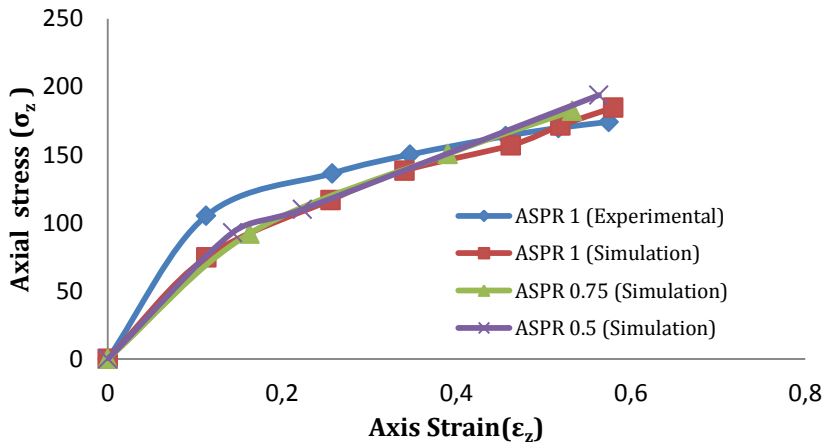


Fig. 5 The relationship between axial stress σ_z and axial strain ϵ_z

Fig. 6 shows the relationship between the hoop stress, σ_θ and the axial strain, ϵ_z for various stress states such as the plane stress and the triaxial stress state conditions. As the axial strain increases, the hoop stress also increases for both the triaxial stress state condition as well as the plane stress condition. However, the hoop stress in the case of triaxial stress state is more when it is compared to the plane stress condition. A similar trend is observed in the simulations as well, and the difference between the experimental and the simulated results is much less as is evident from Fig. 6. The hoop stress was found to increase with the decrease in the aspect ratio.

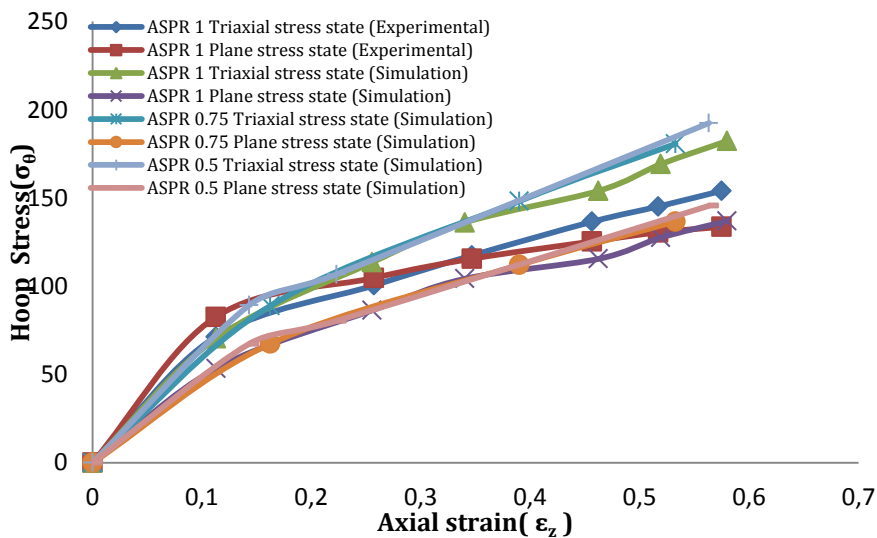


Fig. 6 Hoop stress σ_θ versus axial strain ϵ_z

Fig. 7 shows the relationship between the hydrostatic stress, σ_m and the axial strain, ϵ_θ . In various stress states such as the plane stress and the triaxial stress state conditions, it is noted from the graph that as the axial strain increases, the hydrostatic stress also increases in both the triaxial stress state and the plane stress states. Also, it is observed that the hydrostatic stress is tensile in nature in the triaxial stress state condition, and compressed in the nature in the plane stress state condition. The simulation values are closer to the experimental values in both conditions. The nature of the curve is found to be the same for all the aspect ratios. Additionally, the same trend is seen for the triaxial as well as the plane stress states. The hydrostatic stress is higher in the triaxial stress state condition when compared with the plane stress state condition. The hydrostatic stress is higher for lower aspect ratios.

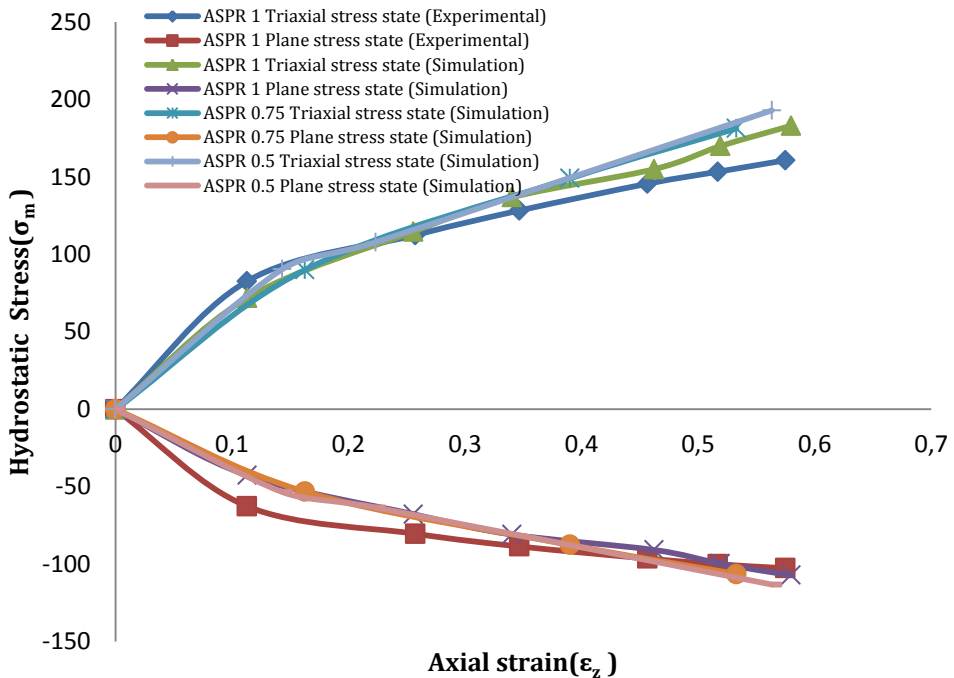


Fig. 7 Hydrostatic stress σ_m versus axial strain ϵ_z

Fig. 8 shows the relationship between the formability stress index and the axial strain in the triaxial stress state condition for both the experimental and the simulation values. It is observed from the graph that the formability stress increases rapidly with the increase in the axial strain. The simulation results have followed the same trend as that of the experiments. Irrespective of the aspect ratio, the formability stress was similar up to 0.15 axial strain. The formability stress index is lower for lower aspect ratio when compared to higher aspect ratios.

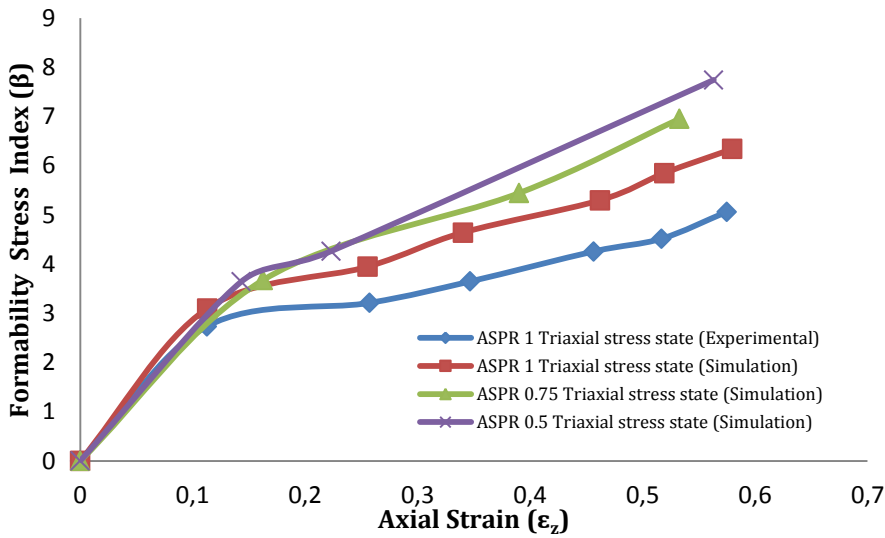


Fig. 8 Formability stress index (β) versus axial strain ϵ_z in triaxial stress state condition

Fig. 9 shows the graph drawn between the formability stress index to axial strain for experimental as well as for the simulation values. It is noticed from the graph that the formability stress increases with an increase in the axial strain initially, and remains constant at the end of the process in the plane stress state condition. A close trend is observed between the experimental and the simulation values. The formability stress index is found to vary very little with the aspect ratios.

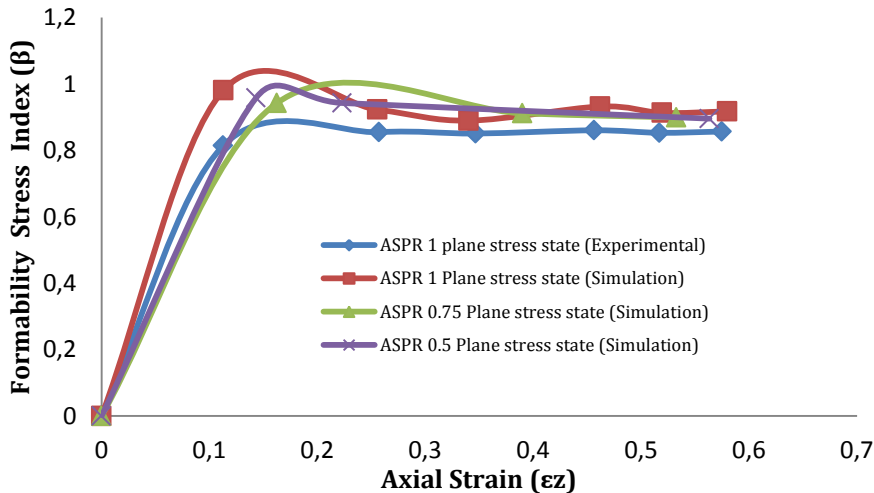


Fig. 9 Formability stress index (β) versus axial strain ϵ_z in plane stress state condition

Fig. 10 shows the formability strain index to axial strain in plane stress state condition. It is noticed from the graph that the formability stress increases with an increase in the axial strain initially, and remains constant at the end of the process in the plane stress

state condition. A close trend is observed between the experimental and the simulation values. The formability strain index does not seem to vary much with the aspect ratios.

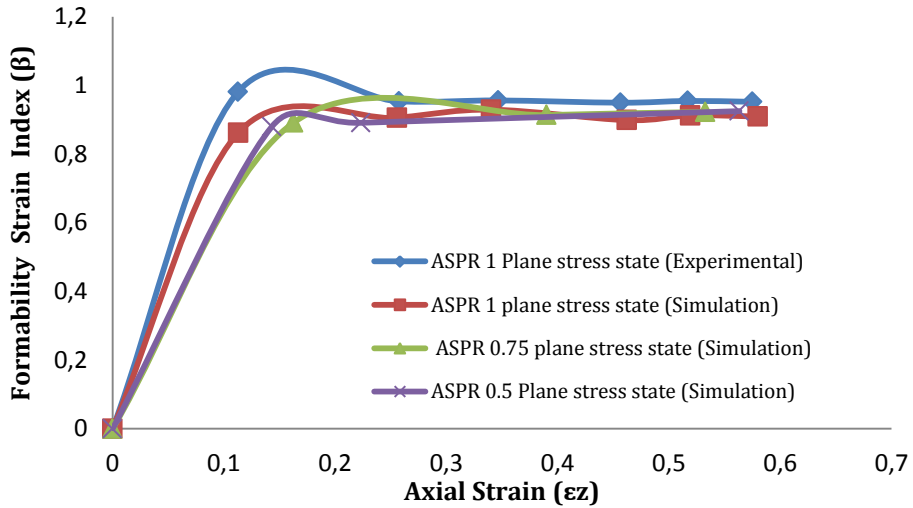


Fig. 10 Formability strain index (β) versus axial strain ϵ_z in plane stress state condition

Fig. 11 shows that the density increases with an increase in the height reduction (%). Moreover, it is observed from the figure that the simulation values are closer to the experimental values irrespective of the aspect ratio of the samples tested. The relative density increases with a decrease in the aspect ratio. The increase in the density is due to the closure of pores from the compression tests. The slow rate of densification for higher aspect ratio samples is due to the presence of higher number of pores in the samples compared to the smaller aspect ratio samples.

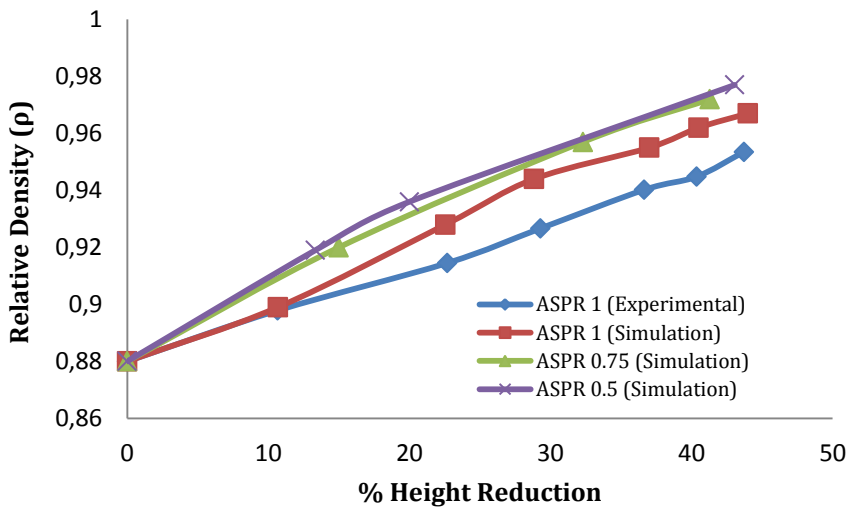


Fig. 11 Relative density (ρ) versus height reduction (%)

Fig. 12 has been drawn between the relative density and the axial strain for the samples of three different aspect ratios namely 1, 0.75 and 0.5. The relative density increases as the axial strain increases for all the aspect ratios. For small aspect ratios, the higher is the relative density; and for higher aspect ratios, the lower is the relative density. The difference in density between samples with aspect ratio 0.75 and 0.5 is found to be very narrow. The closure of pores by the deforming compressive load is said to be the reason for increased densification of the preforms.

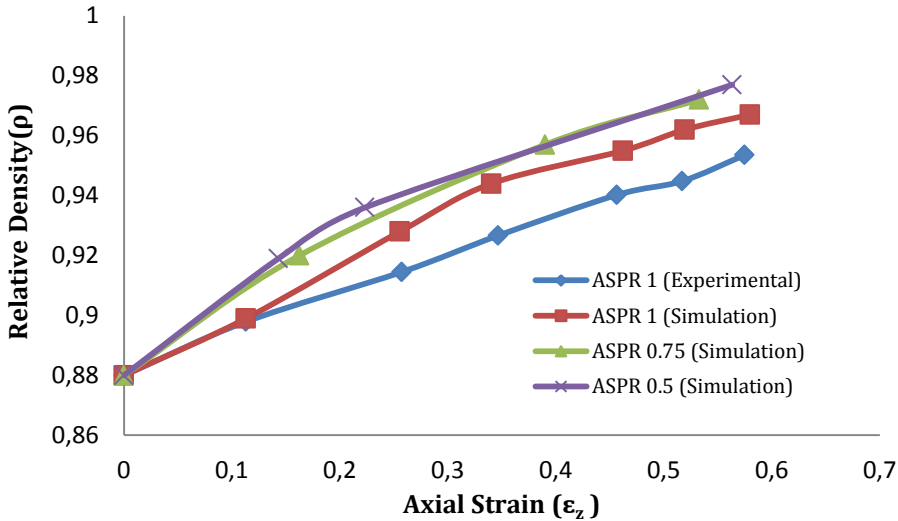


Fig. 12 Relative density (ρ) versus axial strain (ϵ_z)

The Poisson's ratio of a P/M compacts is found to vary with deformation because of its porous nature. Fig. 13 shows the relationship between the Poisson's ratio and the relative density for both the experimental and the simulation values. The Poisson's ratio is found to increase very rapidly in the initial stage of the deformation process. However, during this period, the densification achieved was very little as it is evident from the plot. This may be due to the non initiation of pore closure, as in the initial stages of deformation, the deformation load might have been spent in overcoming the friction in the die preform interface. Once this resistance is overcome, with an increase in load, more pores will be closed resulting in more density and also an increase in Poisson's ratio. However, the change in Poisson's ratio at this stage of deformation was not rapid, but was slow and steady. This is because, during this phase of the deformation, more or less even change in the linear and lateral dimensions of the preforms was encountered. Hence, a steady change in Poisson's ratio was seen in the graph. This trend was seen for preforms of all aspect ratios. The simulation results were found to match the experimental values for all the cases discussed above.

Fig. 14a shows the density of the deformed work-piece across its cross section from the top to its bottom after the end of the simulation cycle. The density is found to be high at the die contact interfaces, and also at the center of the billet. The density is found to be less in the bulge area as the pore closure will be less at these places. The workpiece will be pushed out from the periphery of the die by the metal that is deforming from the metal that is available in the center. Once, the metal is pushed out, the load that acts on its mass will be less, as it will no longer be on the direct contact line of the die. This is evident from the velocity plot given in Fig. 14b. The velocity of the metal flow is found to be high

at the top portion of the preform, and the direction of the flow is found from the center of the preform towards the outer periphery. The velocity lines are found to converge in the bulge portion of the preform. Moreover, at the die preform interface, the velocity is found to be less that is available in the center of the preform. This is due to the presence of frictional resistance between the die and the preform at its interface.

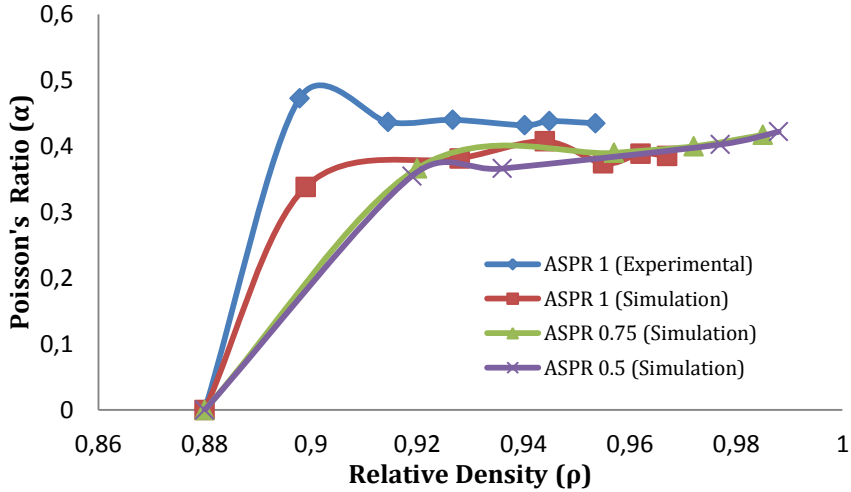


Fig. 13 Poisson's ratio (α) versus relative density (ρ)

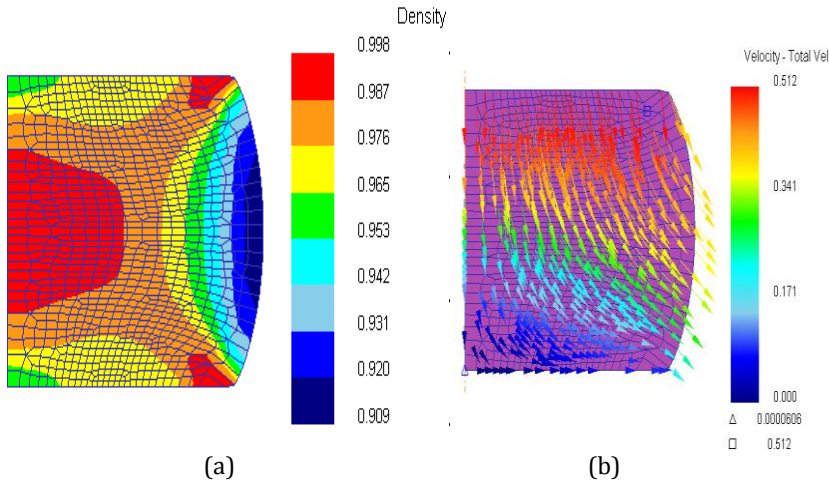


Fig. 14 Distribution of density (a) and material flow rate or velocity of material (b)

4. Conclusions

The densification studies on sintered aluminium preforms were done through experiments as well as through simulations. The simulations performed were found to match the experimental results within acceptable error limits. The following conclusions have been drawn from the analysis performed.

- In both the triaxial and plane stress state conditions, the hoop stress increases with an increase in the axial stress. The hoop stress in the triaxial stress state condition was found to be more than that of the plane stress state condition.
- It is found that the hydrostatic stress is tensile and compressive in nature in triaxial and plane stress state conditions respectively, and followed the same trend for all aspect ratios. The hydrostatic stress is more in triaxial stress state condition than the plane stress state condition.
- The formability stress index is found to increase with the axial strain. It is higher for lower aspect ratio preforms than the higher aspect ratio preforms, and also follows the same trend for all the aspect ratios in triaxial stress state condition.
- In the plane stress state condition, the formability stress and formability strain increase with the increase in the axial strain initially, and remains constant at the end of the process.
- The relative density increases with an increase in the % height reduction. For lower aspect ratio and slow rate of densification, the final density is more due to more number of pores in the sample.

Nomenclature

D_0 Initial contact diameter

D_b Bulge diameter of the preform after deformation

D_c Contact diameter of the preform after deformation

H_0 Initial height of the billet

H_f Final height of the billet after deformation

k_i Instantaneous strength coefficient

n_i Instantaneous strain hardening exponent

σ_z True axial stress in the axial direction

σ_m Hydrostatic stress

σ_θ Hoop stress

ε_z True axial strain in the axial direction

ε_m Hydrostatic strain

γ Poisson's ratio

α Conventional Poisson's ratio

ρ_0 Initial preform density of the billet

ρ_f Final preform density of the billet after deformation

ρ_{th} Theoretical density of the fully dense material

References

1. Griffiths TJ, Davies R and Bassett MB. Compatibility equations for the powder forging process. *Powder Metallurgy*, 1977; 4: 214 – 220.
2. Sun XK, Chen SJ, Xu JZ, Zhen LD and Kim KT. Analysis of cold compaction densification behaviour of metal powders. *Materials Science and Engineering: A267*, 1999; 43 – 49.
3. Hansen N. Dispersion strengthened aluminium products manufactured by powder Blending. *Powder Metallurgy*, 1969; 12(23): 23 – 44.
4. Kuhn HA and Downey CL. How flow and fracture affect design of preforms of powder forging, *Powder Metallurgy, Powder Technology*, 1974; 10(1): 59 – 66.

5. Narayanasamy R and Ponalagusamy R. A Mathematical theory of plasticity for compressible powder metallurgy materials-Part II. *Journal of Materials Processing Technology*, 2000; 97: 110 – 113.
6. Park JJ. Constitutive relations to predict plastic deformations in porous metal during Compaction *International Journal of Mechanical Sciences*, 1995; 37: 709 – 719.
7. Selvakumar N and Narayanasamy R. Phenomenon of strain hardening behaviour of sintered aluminium preforms during cold axial forming. *Journal of Materials Processing Technology*, 2003; 142: 347-354.
8. Narayanasamy R, Ramesh T and Pandey KS. Some aspects on workability of aluminium-iron powder metallurgy composite during cold upsetting, *Materials Science and Engineering: A391*, 2005; 418 – 426.
9. Zhang XQ, Peng YH and Ruan XY. Simulation and fracture prediction for sintered materials in upsetting by FEM. *Journal of Materials Processing Technology*, 2000; 105: 253 – 257.
10. Huang CC and Cheng JH, An investigation into the forming limits of sintered porous materials under different operational conditions. *Journal of Materials Processing Technology*, 2004; 148: 382 – 393.
11. Chandrasekhar P and Singh S. Investigation of dynamic effects during cold upset-forging of sintered aluminium truncated conical preforms. *Journal of Materials Processing Technology*, 2011; 1285 – 1295.
12. Narayanasamy R, Ramesh T, Pandey KS and Pandey SK. Effect of particle size on new constitutive relationship of aluminium-iron powder metallurgy composite during cold upsetting, *Material and Design*, 2008; 29: 1011 – 1026.